Magnetic Resonance Imaging and Modeling of Flow in Hollow-Fiber Bioreactors

Nuclear magnetic resonance flow imaging (MRFI) was used to measure fluid flow noninvasively in the extracapillary space (ECS) of a hollow-fiber bioreactor without cells. Agreement between these axial flow measurements in a single hollow-fiber module and predicted axial velocity contour plots at various image planes along the path length was good.

Flow in a solid-wall tube (phantom) was first used to calibrate pixel intensities with axial velocities. Flow images at several locations along the permeable hollow fiber length were then obtained in order to observe the well-known leakage or Starling flow in the ECS. These quantitative spatially dependent velocity measurements were then compared to theoretically derived velocities obtained from a solution of Poisson's equation with a constant pressure gradient and no slip at the solid surfaces. A mathematical transformation was used to simplify the numerical methods. Leakage flow through the ECS of a multifiber bioreactor (40 fibers) was also measured by MRFI, illustrating the applicability of this method for optimizing operational procedures and design of membrane bioreactors and filtration devices.

C. A. Heath
G. Belfort
Bioseparations Research Center
Department of Chemical Engineering
Rensselaer Polytechnic Institute
Troy, NY 12180

B. E. Hammer
S. D. Mirer
Magnetic Resonance Research Laboratory
Intermagnetics General Corp.
Troy, NY 12180

J. M. Pimbley
Department of Mathematical Science
Rensselaer Polytechnic Institute
Troy, NY 12180

Introduction

In recent years, membrane bioreactors have been used extensively for enzyme reactions and the cultivation of yeast, mammalian, insect, and plant cells because of their immobilization and permselective properties (Knight, 1989). Advances in recombinant DNA and cell fusion technologies have led to increasing demands for cost-effective means of processing large quantities of protein products from mammalian and plant cells. Membrane systems have begun to fill this need because they provide:

1. A barrier between cells and flowing medium reducing contamination, the damaging effects of fluid shear stress on fragile cell membranes, and unwanted contamination from the medium.
2. Large surface area per unit volume for substrate delivery and waste removal, leading to high cell densities, high product concentrations, and high volumetric productivities.
3. Ease of use in continuous and recycle systems.
4. Separation of catalyst and product, eliminating one step in costly product purification (Shuler, 1987; Belfort, 1989).

A disadvantage of membrane biocatalytic systems is the occurrence of mass transfer limitations, resulting in low cell viabilities. Depending on variables such as the membrane thickness and permeability, cell region dimensions, and substrate concentrations, transport may occur primarily by diffusion, by convection, or by both. The relative importance of these two types of transport can be assessed easily by calculating the appropriate Peclet number, which is a ratio of convection to diffusion. In an effort to better understand and optimize mass transfer in membrane bioreactors, numerous mathematical models of diffusional transport have been developed for systems containing enzymes (Rony, 1971; Horvath et al., 1973; Waterland et al., 1974; Georgakis et al., 1975; Kim and Cooney, 1976) and whole cells (Webster et al., 1978, 1979, 1981; Davis and Watson, 1985, 1986; Heath and Belfort, 1987). Conversely, only a few studies have been published on convective transport or on simultaneous diffusive and convective transport of nutrients in these systems (Schonberg and Belfort, 1987; Salmon et al., 1988). Only Karel and Robertson (1987), using ^{35}S labeling and autoradiography, have measured spatial variations in the rate of cell growth and cell movement. No one, however, has directly measured the convective leakage flow in the shell space of

Correspondence concerning this paper should be addressed to G. Belfort.
The present address of C. A. Heath is Thayer School of Engineering, Dartmouth College, Hanover, NH 03755.

membrane bioreactors. Convective transport can be advantageous in membrane systems by supplementing diffusion and reducing the potential for mass transfer limitations. However, convection in the extracapillary space (ECS) may also cause catalyst redistribution by dragging the cells or enzymes toward the exiting end of the reactor where they may accumulate at the membrane surface. This nonuniform catalyst distribution is not likely to be optimal for efficient reactor productivity.

This paper attempts to fill that void by providing both the development of mathematical analyses describing convective transport in a membrane system and experimental verification of the nonconcentric simplified model equations using magnetic resonance flow imaging (MRFI). The goal of this work and others like it is not only to further the understanding of mass transfer in membrane bioreactors but also to provide a basis for improving design, operation, and scale-up of membrane systems for a variety of uses.

Theory

Under most circumstances, fluid and substrate transport in the cell region of membrane bioreactors does not occur by diffusion alone. Convection through the membrane into and from the extracapillary cell region (Starling flow) also provides a contribution that supplements the diffusive transport (Starling, 1896). These convective effects have been modeled by the method of Apelblat et al. (1974), who described fluid flux in capillaries and tissues. The change in direction of transmembrane flux from the arterial to the venous system in the capillary bed is analogous to that in a membrane bioreactor system. Fluid from the lumen enters the ECS through the hollow-fiber membrane near the reactor inlet due to the pressure drop in that direction. With a closed ECS, the pressure drop is in the opposite direction in the exit half of the reactor, forcing the fluid from the ECS to return from the ECS to the fiber lumen, where it flows out of the reactor. This leakage or Starling flow usually constitutes only a small percent of the bulk axial flow within the fiber lumen.

Two approaches are taken here The first approach, which we call the *comprehensive model,* follows the Apelblat et al. (1974) formalism but uses permeability coefficients for immobilized cells rather than tissue and a microporous polysulfone membrane rather than a dense membrane. We have also included the option of examining anisotropic effects in the membrane, that is, $k_{21} \neq k_{22}$, and assume that the single hollow-fiber membrane is placed axisymetrically in the ECS. Flow in the cell-containing ECS is described by a Darcy law and is characterized by a Darcy constant or permeability coefficient k_3. In the second approach, which we call the *simplified model,* we consider only two-dimensional flow with continuity in the ECS in which the single hollow-fiber membrane is *not* placed axisymetrically and in which cells are absent. We obtain two-dimensional contour plots of axial velocity which are then compared with the MRFI measurements.

Comprehensive model

The development of the appropriate model equations describing Starling flow will be presented in brief. The reader is directed to Apelblat et al. (1974) for the complete analysis. For a hollow-fiber membrane bioreactor (HFBR) the theory begins with the simplified equation of continuity

$$(\nabla \cdot \mathbf{V}) = 0 \tag{1}$$

where boldface type indicates a vector quantity, and the equation of motion (constant density and viscosity) governing fluid flow in the lumen is

$$\frac{\partial \mathbf{V}}{\partial t} + (\mathbf{V} \cdot \nabla)\mathbf{V} = -\frac{1}{\rho}\nabla \mathbf{P} + \nu \nabla^2 \mathbf{V} + \mathbf{F} \tag{2}$$

where ρ is density, $\mathbf{P}$ is pressure, ν is kinematic viscosity, and $\mathbf{F}$ represents body forces. Also necessary is Darcy's law, which relates fluid permeation velocity for creeping flow and the applied pressure gradient in the porous membrane and cell (ECS) regions:

$$\mathbf{V} = -k\nabla \mathbf{P}/\bar{\eta} \tag{3}$$

where k is permeability and $\bar{\eta}$ is fluid viscosity. Diffusive transport is not considered under the assumption that it is negligible compared to convection.

The following development of equations describing convective leakage flow in a concentrically located hollow-fiber system utilizes additional assumptions of steady laminar flow, time independence, negligible body forces ($\mathbf{F} = 0$), and an isotropic, porous cell region in the ECS which can be characterized by a permeability coefficient k. Because only dilute solutions are considered, osmotic effects can be ignored. End effects are also neglected because the aspect ratio of path length to fiber diameter is large. A diagram of the single-fiber system, defining variables and the coordinates, is shown in Figure 1. Using the assumptions mentioned above, Eqs. 1 and 2 simplify in cylindrical coordinates to the following.

$$\frac{\partial P_1}{\partial z} = \bar{\eta}\left(\frac{\partial^2 v_1}{\partial r^2} + \frac{1}{r}\frac{\partial v_1}{\partial r}\right) \tag{4}$$

$$\frac{\partial P_1}{\partial r} = 0 \quad \text{or} \quad P_1 = P_1(z) \tag{5}$$

$$\frac{\partial^2 P_2}{\partial r^2} + \frac{1}{r}\frac{\partial P_2}{\partial r} + \frac{\partial^2 P_2}{\partial z^2} = 0 \tag{6}$$

$$\frac{\partial^2 P_3}{\partial r^2} + \frac{1}{r}\frac{\partial P_3}{\partial r} + \frac{\partial^2 P_3}{\partial z^2} = 0 \tag{7}$$

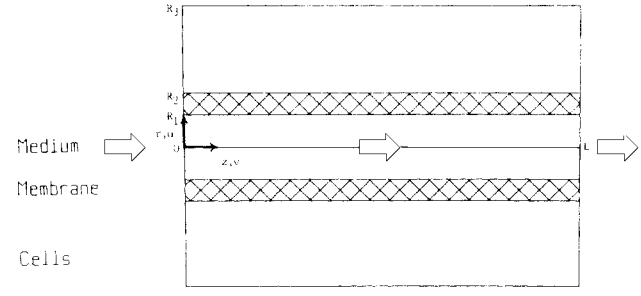

Figure 1. System definition for modeling convective flow in a concentrically located hollow-fiber bioreactor.

where $\bar{\eta}$ is viscosity, v is axial velocity (in the z direction), and subscripts 1, 2, and 3 refer to lumen, membrane, and extracapillary regions, respectively. The applicable boundary conditions in the lumen region are

$$P_1(r, 0) = P_0 \tag{8a}$$

$$P_1(r, L) = P_L \tag{8b}$$

$$v_1(R_1, z) = 0 \tag{8c}$$

$$\frac{\partial v_1(r = 0)}{\partial r} = 0 \tag{8d}$$

$$u_1(0, z) = 0 \tag{8e}$$

where u is radial velocity (in the r direction). Equation 8c indicates no slip at the membrane surface and Eqs. 8d and 8e reflect flow symmetry in the fiber lumen. The boundary conditions at the lumen-membrane and membrane-cells interfaces are

$$u_1(R_1, z) = u_2(R_1 z) \tag{9a}$$

$$P_1(R_1, z) = P_2(R_1 z) \tag{9b}$$

$$u_2(R_2, z) = u_3(R_2 z) \tag{9c}$$

$$P_2(R_2, z) = P_3(R_2 z) \tag{9d}$$

$$v_3(R_2, z) = 0 \tag{9e}$$

Equation 9e is again the no-slip condition. Since the system for $R_1 < r < R_3$ is closed at the two ends ($z = 0, L$), the following restrictions also apply

$$v_2(r, 0) = v_3(r, 0) = 0; \quad R_1, < r < R_3 \tag{10a}$$

$$v_2(r, L) = v_3(r, L) = 0; \quad R_1, < r < R_3 \tag{10b}$$

$$u_3(R_3, z) = 0 \tag{10c}$$

From Eq. 1 we have

$$\frac{\partial v_1}{\partial z} + \frac{\partial u_1}{\partial r} + \frac{u_1}{r} = 0 \tag{11}$$

and from Darcy's law follows

$$v_2(r, z) = -\frac{k_{22}}{\bar{\eta}} \frac{\partial P_2}{\partial z} \tag{12}$$

$$u_2(r, z) = -\frac{k_{21}}{\bar{\eta}} \frac{\partial P_2}{\partial r} \tag{13}$$

$$u_3(r, z) = -\frac{k_3}{\bar{\eta}} \frac{\partial P_3}{\partial r} \tag{14}$$

where k_{21} and k_{22} are the membrane permeabilities in the r and z directions, respectively. The two permeabilities are equivalent ($k_{21} = k_{22} = k_2$) when the membrane is isotropic. The pressure distributions in the membrane and extracapillary regions ($i = 2$, 3) are given by (Apelblat et al., 1974):

$$P_i(r, z) = A + B\left[L/2 + \sum_{n=1}^{\infty} C_n F_i(\alpha_n r) \cos(\alpha_n z)\right] \tag{15}$$

The volumetric flow rate $Q_3(z)$ into region 3 from the entrance to a distance z in the reactor is given by

$$Q_3(z) = -\frac{2\pi R_2 k_3 B}{\bar{\eta}} \sum_{n=1}^{\infty} C_n X_3(\alpha_n R_2) \sin(\alpha_n z) \tag{16}$$

The detailed solution obtained from Eqs. 4–11 with Eqs. 12–15 is presented in the appendix.

Nonconcentric simplified model

In order to verify both the magnetic resonance flow measurement and the premises inherent in our formulation, we claim that it is important to compare the theoretical Starling flow with the measurement in the extracapillary space. Unfortunately, it is difficult to place the porous hollow fiber concentrically within the large cylinder. Hence, the flow within this *annulus* depends on the angular coordinate and an analytical solution does not appear to be feasible.

A numerical finite-difference program to treat this problem has been developed. The appropriate formulation is that described by Apelblat et al. (1974) for laminar steady flow in which nonlinear terms vanish. The simplified problem we wish to solve is Poisson's equation

$$\nabla^2 v(x, y) = -1 \tag{17}$$

where v is the cylindrical (i.e., radial and angular) distribution of the axial velocity in the geometry of Figure 2. Note that -1 has been substituted for the pressure gradient since the computation will eventually be scaled to equate the maximum axial velocity of the model to that of the experiment. The axial dependence in the Eq. 17 formulation has been omitted since this dependence is expected to enter only as a scale factor through continuity. That is, the annular axial velocity increases as fluid flows radially from the hollow fiber into the annulus along the entrance half of the fiber and decreases as the fluid flows back into the hollow fiber from the annulus along the exit half of the fiber, but to first order the radial and angular dependences of the axial velocity do not change. We have also scaled the lengths such that the radius of the outer cylinder is unity and the (normalized) radius to the exterior wall of the membrane is now a. The boundary conditions are the conventional *no-slip* specification that the axial velocity vanishes on the inner and outer boundaries of the ECS.

With reference to Figure 2, the inner cylinder (hollow fiber) has radius a and off-center displacement μ. We could discretize this two-dimensional domain immediately and proceed with the numerical solution. But we insert another idea here to expedite the numerical calculation. Let us define the physical domain of Figure 2 as the z plane with Cartesian coordinates x and y. (The problem will be solved in cylindrical coordinates, but it is helpful to refer to Cartesian coordinates in the present discussion).

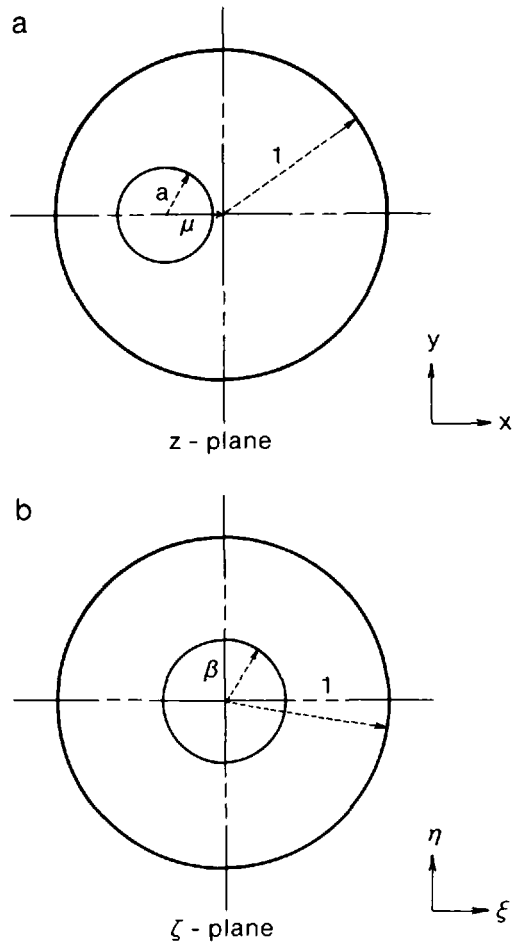

(a) Off-Center (z plane)
(b) On-center (ζ-plane)

Figure 2. Location of inner hollow fiber.

Next, ζ is defined as an analytical function of z such that

$$\zeta = \frac{z - \alpha}{1 - \alpha z} \tag{18}$$

with

$$\alpha \equiv \frac{-(1 - \mu^2 - a^2)}{2\mu}\left[1 - \sqrt{1 - \left(\frac{2\mu}{1 + \mu^2 - a^2}\right)^2}\right]$$

Cartesian coordinates enter as the real and imaginary parts of the complex variables z and ζ. That is, $z = x + iy$ and $\zeta = \xi + i\eta$. Equation 18 is a transformation in the complex plane The ζ plane representation now has a concentric inner cylinder of radius $\beta = |(\alpha + \mu - a)/[1 + \alpha(\mu - a)]|$. Writing $v(x, y) \equiv V(\xi, \eta)$, the Laplacian transforms as

$$\frac{\partial^2 v}{\partial x^2} + \frac{\partial^2 v}{\partial y^2} \equiv (\xi_x^2 + \xi_y^2)\left(\frac{\partial^2 V}{\partial \xi^2} + \frac{\partial^2 V}{\partial \eta^2}\right)$$

$$= \left[\frac{1 + \alpha^2(\xi^2 + \eta^2) + 2\alpha\xi}{1 - \alpha^2}\right]^2 \left(\frac{\partial^2 V}{\partial \xi^2} + \frac{\partial^2 V}{\partial \eta^2}\right) \tag{19}$$

The factor multiplying the Laplacian in the ζ coordinates is not a function of the radial coordinate (i.e., square root of $\xi^2 + \eta^2$) only. Hence, the exact solution is two-dimensional even though the boundary conditions have the simple one-dimensional form. The transformation essentially shifts the two-dimensional nature of the problem from the domain geometry and boundary conditions to the inhomogeneous term. This shift is highly advantageous for numerical computation. The finite-difference grid is far easier to construct since the domain is now rectangular in cylindrical coordinates. The finite-difference method converts the linear partial-difference equation to a linear system of algebraic equations to which we apply a standard sparse matrix solver.

Simulations

Comprehensive model

Simulations from the model equations of convective leakage flow in a hollow-fiber bioreactor have been generated using variations of typical dimensions and parameter values from A/G Technology membrane systems (Needham, MA). Values for the membrane permeability were chosen to fall near actual values for two membranes: the polysulfone membranes used in the study have a mean permeability of 2.2×10^{-11} cm^2 while the polyvinylidene diflouride (Durapore, Millipore) membranes have a mean permeability of 1×10^{-5} cm^2. The permeability of water in the empty ECS was taken to be 1 cm^2 while the permeability of tissue has been described as 1×10^{-14} cm^2 (Apelblat et al., 1974). Since the concentration of cells in tissue ($>10^9$ cells/mL) is higher than the cell concentration in immobilized bioreactors ($\sim 10^8$ cells/mL), then permeability through immobilized cells is assumed to be greater than through tissue but not nearly as high as through a cell-free compartment. Figure 3 shows flow streamlines in the extracapillary space of a hollow-fiber reactor (entrance half only). As indicated, the flow is primarily axial, with radial components at the ends and at the membrane surface. Because of the nature of the computational method and the adsorbed no-slip condition, Eq. 9e, the simulated profiles show straight line segments at a few locations when in reality the streamlines should consist solely of curves. The second half of the system (not shown) depicts a mirror image of flow with the streamlines curving toward the membrane surface near the reactor exit. The constant-pressure lines (isobars), not shown, are perpendicular to the flow streamlines, forming an orthogonal net. The value of 1 cm^2 for the permeability in the cell region corresponds to that of fluid without cells.

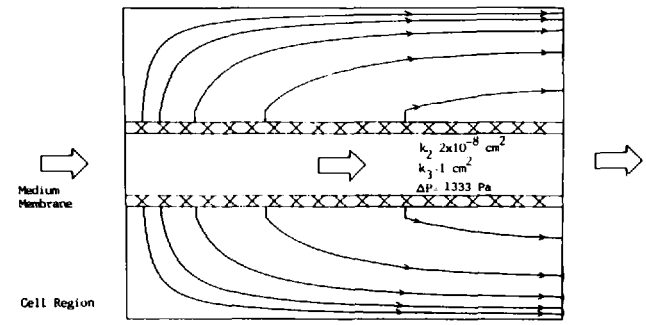

Figure 3. Simulated streamlines of leakage flow in cell region of a concentrically located hollow-fiber bioreactor.

Figures 4 and 5 demonstrate how axial and radial velocity, respectively, vary in the cell region from the membrane surface to an outer boundary (the cartridge) for the case of very high permeability in the ECS ($k_3 = 1$ cm^2). Axial velocity, Figure 4, varies from zero at the membrane surface due to the no-slip condition to a maximum at a point in the annulus between the two cylindrical surfaces and then decreases to zero at the outer wall. The simulated axial velocity profiles correspond to three different locations along the fiber. The maximum axial flow occurs at the hollow fiber midpoint as expected, since the flow is entirely axial at this location. The radial velocity, Figure 5, shows a maximum at the membrane surface and continually decreases to zero at the outer wall. The radial velocity profiles, taken at four locations along the fiber length, demonstrate that the radial component of velocity in the cell region is highest near the reactor entrance, decreasing to zero at the reactor midpoint.

The variation of leakage flow into the extracapillary space containing cells with membrane thickness and permeability for the hollow-fiber system is shown in Figure 6 for the case of very low permeability in the ECS ($k_3 = 10^{-10}$ cm^2). Assuming an isotropic membrane, a decrease in permeability and an increase in membrane thickness both result in decreased leakage flow as expected. When membrane and cell region permeabilities are equal, membrane thickness has little effect on leakage flow; however as the membrane permeabilities decrease a growing loss of flow in the cell region results from increasing membrane thickness, as seen by the curves in the figure. Thus, membrane thickness is more important in determining the quantity of leakage flow with less permeable membranes.

Figure 7 indicates the variation in the ratio of leakage flow into the cell region to lumen flow as a function of membrane thickness and permeability in the cell region. Since permeabilities of the membrane and cell regions are not significantly different, membrane thickness has little effect. However, an increase in the permeability of the cell region does increase the proportion of leakage to lumen flow. In a functioning bioreactor, as the permeability of the cell region decreases due to increasing cell density, the proportion of leakage to lumen flow may drop

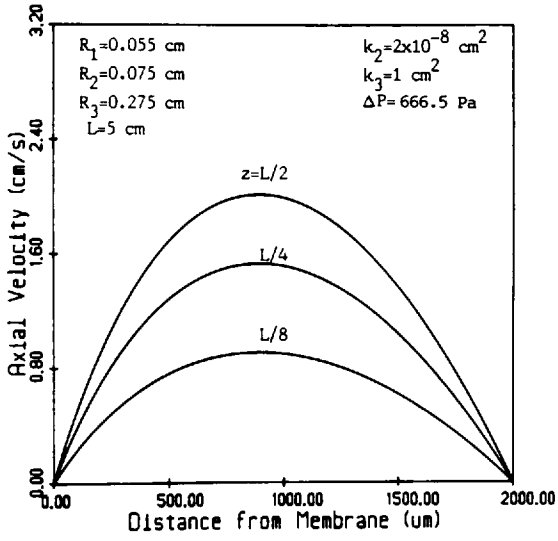

Figure 4. Simulated axial velocity profiles in cell region of a concentrically located hollow-fiber bioreactor.

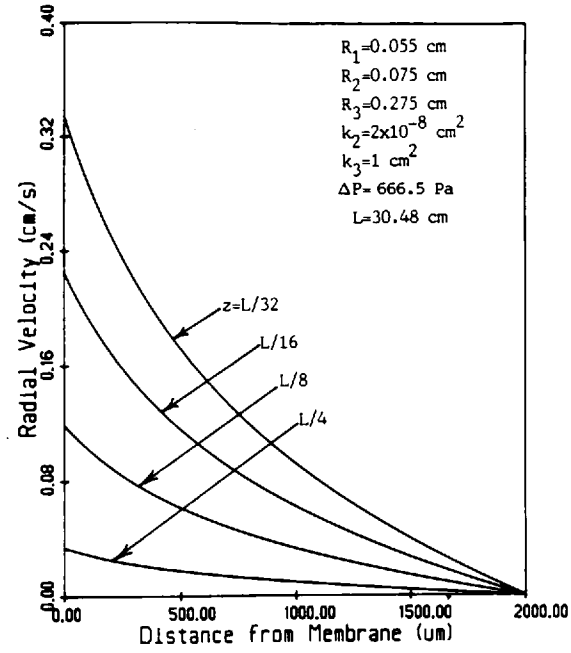

Figure 5. Simulated radial velocity profiles in cell region of a concentrically located hollow-fiber bioreactor.

significantly, reducing the convective transport of molecules to and from the cell region.

Nonconcentric simplified model

Although this problem is somewhat contrived in that most commercial hollow-fiber bioreactors do not have an imperme-

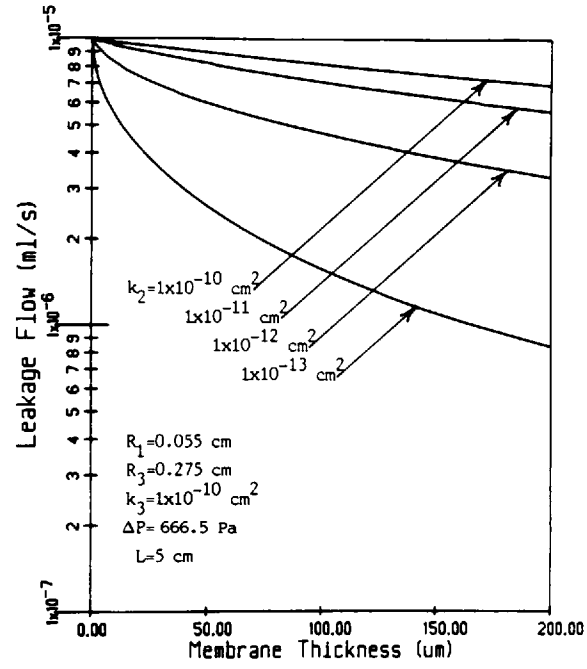

Figure 6. Leakage flow in cell region of a concentrically located hollow-fiber bioreactor v. membrane thickness for various values of membrane permeability.

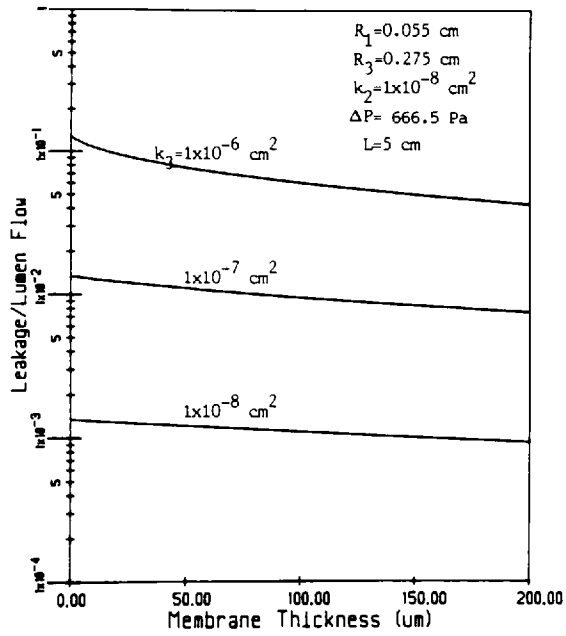

Figure 7. Ratio of leakage flow in cell region to lumen flow for a concentrically located hollow-fiber bioreactor v. membrane thickness for various values of cell region permeability.

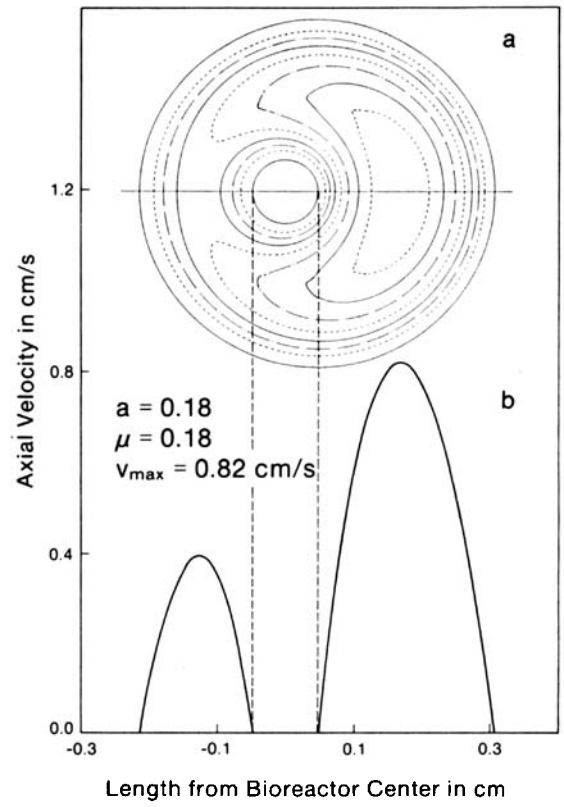

Figure 8. Simulated axial velocity in extracapillary space at a fractional axial distance of 0.534.
(a) As a contour plot
(b) As a function of radial coordinate

able cylinder of finite radius surrounding each hollow fiber, the experiments for the single-fiber module did employ such a structure. So for the purposes of validation, the appropriate nonconcentric simplified model is compared with the experimental data. One bioreactor manufacturer (Setec, Inc., Livermore, CA) does, however, sell a membrane module with a smaller diameter hollow fiber inserted into a larger diameter hollow fiber. The biocatalyst (cells) is placed in the annulus between the fibers. For this case, our results are directly applicable.

Equations 17 and 19 are solved numerically to obtain the plots shown in Figure 8. Equal flow contours for the axial velocity within the annulus (in the z plane) or extracapillary space are shown for the nonconcentrically positioned hollow-fiber case where $\mu = 0.18$ and at a fractional axial distance of 0.534. A quantitative measure of the axial velocities at each location along the diameter cross section (horizontal line) is obtained and shown in Figure 8b for the same conditions.

Experimental Method

Flow images were obtained by spatial phase encoding of flow via a modified spin warp imaging sequence (Moran, 1982). The sequence is shown in Figure 9. In this technique, a spin warp pulse sequence (Edelstein et al., 1980) was used with a bipolar z gradient to achieve slice selection and to phase encode spins having a z component of flow (i.e., flow normal to the imaging plane). A series of phase-encoded two-dimensional images was obtained by incrementing the bipolar z gradient for each image. The acquired data set is three-dimensional. The first two dimensions encode space, the third dimension is flow. A three-dimensional Fourier transformation of the data yields a series of two-dimensional images in which each image shows the location of fluid with a dispersion of velocities within a velocity window. The total velocity range is determined by the strength of the z gradient whereas the resolution (i.e., distribution of velocities within the window) depends upon the number of z-gradient encodings. Orthogonality of flow encoding is maintained because phase shifts occur only when the flow vector component is colinear with the direction of the gradient. Since a bipolar gradient is used only in the z (axial) direction, only axial flow components are phase encoded (Nishimura et al., 1986).

A hollow-fiber bioreactor can typically be characterized by two groups of flow velocities. Very fast flow occurs inside the hollow-fiber lumens and slow Starling flow is present in the

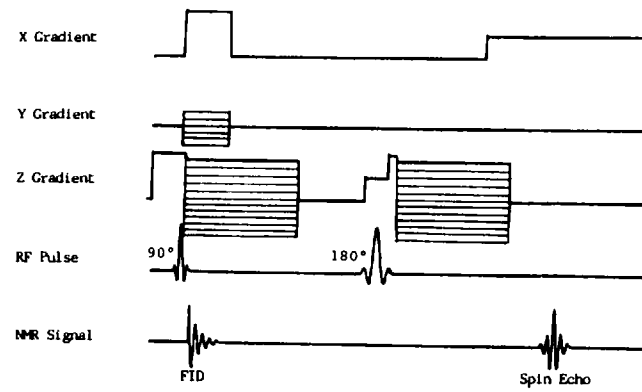

Figure 9. MRFI pulse sequence used for obtaining flow images by spatial phase encoding of flow via a spin warp imaging sequence.

extracapillary space. Starling flow is between one and two orders of magnitude smaller than axial lumen flow. This presents a large range of flow velocities to measure. Because the slow Starling flow in the extracapillary space is of primary interest, the range of detectable velocities was limited to those of Starling flow by employing a selective 180° RF pulse as a flow velocity filter, Figure 9. Spins that flow out of the imaging plane before the selection 180° pulse is applied will not be detected. The range of flow velocities is a function of the time delay between the 90° and 180° RF pulses and of slice thickness. Restricting the range of measurable velocities by this method assures that fast flow components will not be aliased back into the flow image. The technique is useful for velocities greater than the diffusion of water up to velocities of 100 cm/s. The velocity range studied is dependent on gradient strength and gradient switching times. In this study, the gradient strength, spin echo, and gradient on times were optimized for the flow encountered.

The hollow-fiber module was part of a recirculation system, Figure 10, that maintained steady nonpulsatile flow. This was necessary for accurate velocity measurements and prevention of motion artifacts in the images. Distilled water doped with cupric chloride (1 g/L) to reduce the data acquisition time was used for measuring the axial velocity as a function of location in the bioreactor ECS. The proton NMR data were collected on a modified Seimco spectrometer (Seimco Inc., New Kensington, PA) connected to a 25 cm warm bore superconductive magnet (Intermagnetics General Corp., Guilderland, NY) operated at 2.1 Tesla. The signals were reconstructed using three-dimensional Fourier transformation techniques. Pixel intensities in the spatial images were related to velocity via calibrated flow phantoms.

Phantom

A nonpermeable glass tube (8.1 mm ID, 225 mm long) was used in place of the hollow-fiber module to calibrate the flow images obtained from the MRFI data. The image was obtained for a constant flow rate of 15 mL/min, which yielded a range of velocities from 0 to 10 mm/s, providing a calibration of pixel intensities to velocity for use in describing Starling leakage flow in the hollow-fiber modules.

Single-fiber module

A module containing a single hollow fiber was specially constructed by A/G Technology (Needham, MA) for use in this part of the study. A microporous polysulfone fiber, with a pore size of 0.2-μm and 1.1 mm ID was potted in a cartridge 58 cm long with approximately 0.6 cm ID. The flow in the single-fiber module was maintained at 150 mL/min. Images were taken at five locations along the fiber length to observe the Starling flow distributions at these points (4.3, 6.7, 10.5, 10.7, and 31.0 cm from the reactor entrance). Locations are given at fractional axial distances in Table 1.

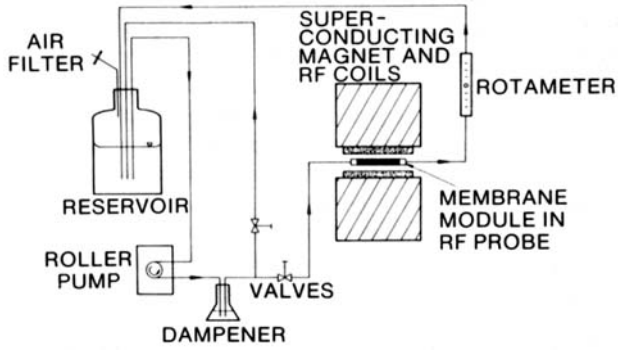

Figure 10. Diagram of flow system used in MRFI of Starling flow in membrane bioreactors.

Multiple-fiber module

A module containing 40 fibers with a molecular weight cutoff of 100,000 (UFP-100-E-3, A/G Technology, Needham, MA) was used to image leakage flow in a multiple-fiber system. Images were acquired under flow (250 mL/min) and zero flow conditions.

Results

Phantoms

Figure 11a demonstrates the contour plot of velocity inside the glass tube with a flow rate of 15 mL/min. Each contour line was derived from one flow image, representing a particular velocity. Each contour line in the plot corresponded to a radial location in the glass tube for which velocity was easily determined using the equation for a parabolic velocity profile,

$$v(r) = 2Q(1 - (r/R)^2)/\pi R^2 \qquad (20)$$

where Q is flow rate and R is the inner radius of the tube. The resulting profile described by Eq. 20 and the data points corresponding to the contour lines are shown in Figure 11b. This process permanently assigned to each contour line (and its corresponding image) a particular velocity which was then used to determine velocity as a function of radial distance in the single-fiber module.

Single-fiber module

The theoretical analysis of convective leakage flow in the extracapillary space of a hollow-fiber module was developed assuming that the membrane was centered in the unit. The actual module used for experiments contained a fiber that was not accurately centered, resulting in an off-center displacement in the location of the fiber along the reactor length. To account for this asymmetry, a nonconcentric simplified model was developed. Simulation results from this model showing equal flow contours for the axial velocity at different z planes along the path length and within the extracapillary space are overlaid on

Table 1. Summary of Data Used for Simulations

Figure No.	Fractional Axial Distance*	Off-Center Displacement μ**	Peak Axial Velocity cm/s
8	0.534	0.18	0.82
12a, 13a	0.293	0.15	0.74
12b, 13b	0.181	0.37	0.57
12c, 13c	0.116	0.24	0.45
12d, 13d	0.074	0.10	0.32

*Fiber length 58 cm

**Values are fractions of the cylinder radius $R = 0.27$ cm. These values can be taken from the MRFI measurement. We did not use them as fitting parameters; the only adjustable parameter is peak velocity.

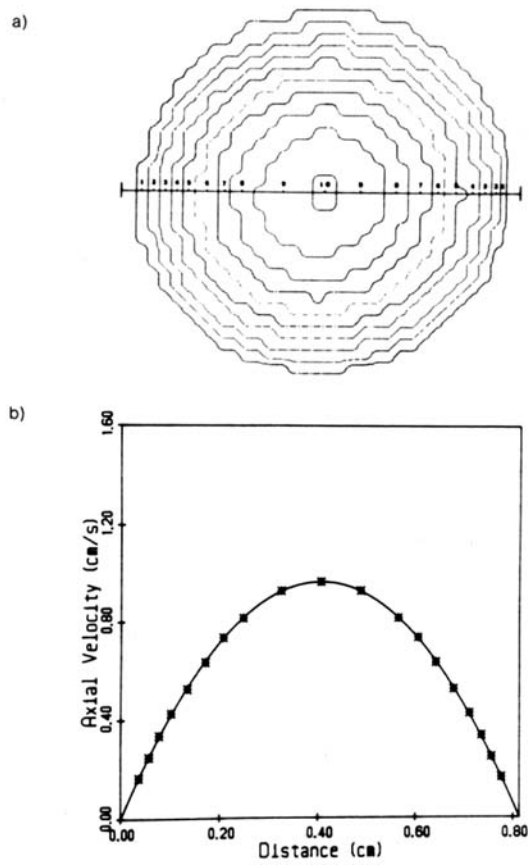

Figure 11. Flow phantom.

(a) Contour plot of velocity as found by MRFI
(b) Corresponding parabolic velocity profile calculated from known flow rate

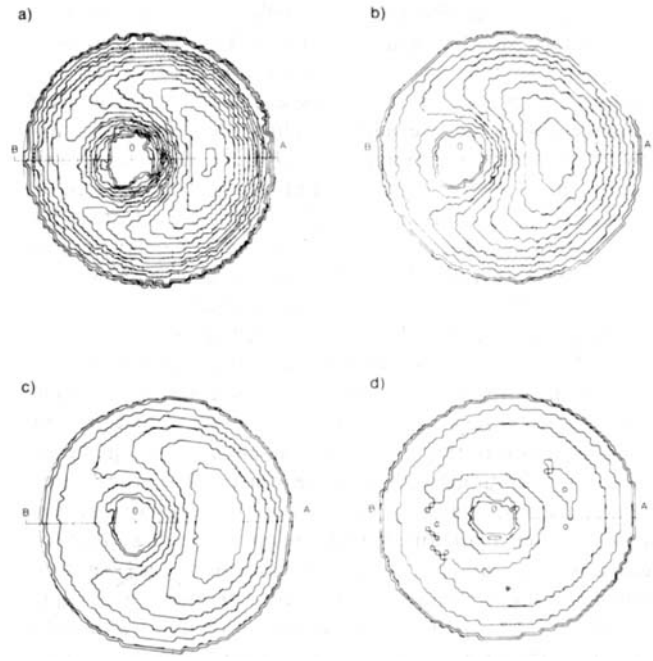

Figure 12. Simulated axial velocity contour plots in extracapillary space overlaid on magnetic resonance flow images at various fractional axial distances.

—, ----, — - — Contour plots; dark irregular lines are MRF images
Fractional axial distances: (a) 0.293, (b) 0.181, (c) 0.116, (d) 0.074
see Table 1 for maximum velocities and off-center distances

the experimental measurements and depicted in Figure 12. The agreement in terms of the shape and position of the contours is very good. Also shown, in Figure 13, are the simpler comparisons of the axial velocity versus radial coordinate for a constant angular coordinate (*O-A* cross section) at the same z planes. Once again, the model predicts the observations well. In these figures the model calculations have been normalized to a single point maximum axial velocity observed in the experiment. In Figure 14 the contour plots are combined with the radially dependent velocity plots along the diameter. The same maximum axial velocity was used for each related model prediction in Figures 12 through 14. Also note that the off-center displacement, μ, varies with axial distance ζ, as seen in Table 1 and Figures 12–14. The reason for this is that the flexible hollow fiber bows along its axis and is unable to maintain a fixed position with distance. A comment regarding what appear to be missing data near the maximum velocities in Figure 13 b, c is appropriate. Both the process of contouring with only a few velocity levels and insufficient flow resolution result in a lack of experimental points near the maximum velocities. Each velocity point in the graph represents the weighted average of a range of velocities in the velocity window.

Multiple-fiber module

Since a functional membrane bioreactor contains more than one hollow fiber, flow images of a module containing 40 fibers under conditions of non flow and flow (250 mL/min) were acquired and are shown in Figure 15. Darker areas in the image indicate higher velocities. The very dark circles demonstrate the fast-moving fluid in the fiber lumens. The velocities corresponding to Starling leakage flow are less, by nature. Notice how the higher velocities (channeling) occur in areas between or among fibers where there is less resistance to flow. A mathematical analysis of this phenomenon was not undertaken in this study.

Discussion

As discussed earlier, diffusion alone is often insufficient to provide adequate mass transfer of substrates to (and wastes from) the bed of densely packed cells in membrane bioreactors. Due to the changing transmembrane pressure difference along the membrane path, convection (Starling leakage flow) into the cell region can enhance the system mass transfer. However, depending on the magnitude of the velocities and the degree of cell attachment, the convective currents in the extracapillary space (ECS) or cell-containing region will cause movement of the cells or catalyst toward the far end of the flow field (Waterland et al., 1975, Tharakan and Chau, 1986), creating an inhomogeneous distribution that has the unwanted effect of impeding mass transfer of nutrients to the cells. When the leakage flows are significent a balance of these two convective effects is necessary for efficient bioreactor operation.

The model equations describing Starling leakage flows in membrane systems developed in this work provide a theoretical basis for this optimization. Acquiring a reliable model to

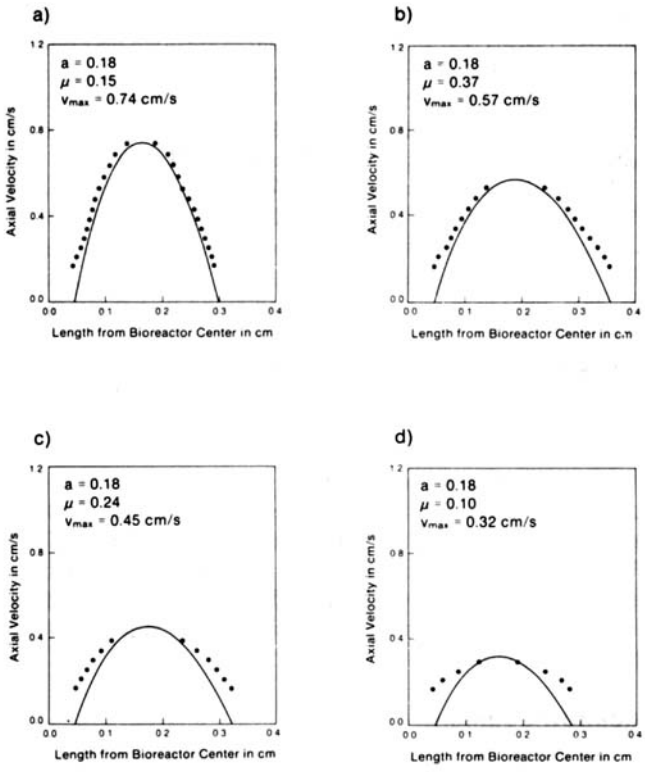

Figure 13. Simulated axial velocity in extracapillary space at various fractional axial distances as a function of radial coordinate.

z-plane maximum velocities and off-center distances μ as in Figure 12 and Table 1

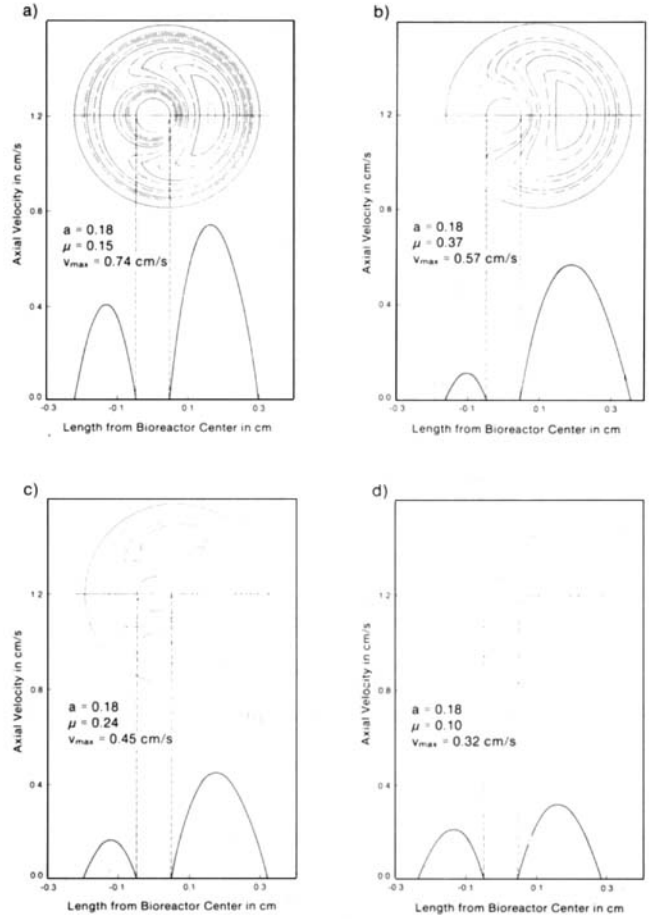

Figure 14. Simulated axial velocity contour plots and radially dependent axial velocity plots.

z-plane maximum velocities and off-center distances μ as in Figure 12 and Table 1

describe fluid velocity in the shell space is the first step toward calculating substrate concentration profiles and cell redistribution in this region. This information can then be used to determine conditions maximizing the benefits of Starling flow.

In this study we have shown that the model yields reasonable results both from a theoretical inspection and from comparison with experimental data. The simulated velocity profiles for the cell region demonstrate the expected results for both the axial and radial directions. Along the length of the fiber, axial velocity is maximum at the module center and radial velocity is highest at the two reactor end points. In the radial direction, the axial and radial velocities have maximum values at a point midway between the membrane and the cartridge wall and at the membrane surface, respectively. While these velocity patterns potentially will provide excellent nutrient transport to cells situated far from the membrane surface, the same flows will relocate suspended cells since the density of a mammalian cell is only slightly greater than that of the culture medium.

Decreasing permeabilities in both the membrane region and the ECS (containing cells) were shown to significantly decrease the quantity of leakage flow. During a bioreactor run cell density generally increases to a maximum value and then remains fairly constant depending on the system conditions. During this time some cell death occurs, creating cellular fragments that increase the packing density of the cells (by filling in the empty spaces between the cells) and which may clog the membrane pores, resulting in decreases in both cell region and membrane permeabilities. Leakage flows will decrease and reduce mass transfer of nutrients, causing further cell death. Although the described sequence of events may be somewhat exaggerated, it demonstrates the interdependent behavior of the state of the cells and the effectiveness of Starling flow. Possible schemes to help minimize the development of necrotic cell regions in the bioreactor by providing a more even distribution of nutrients are to periodically reverse the lumen flow, use pulsatile flow, slowly circulate the cell suspension, and/or to vary the magnitude of the lumen flow. The most effective of these is probably to periodically reverse the direction of the lumen flow since it essentially accomplishes all that the other methods do individually.

The solution to Poisson's equation for axial flow in the extracapillary space with a constant pressure gradient was obtained at each point in a finite-difference grid. No-slip at the solid surfaces and a transformation from the z plane to the ζ plane gave two-dimensional velocity contours that match images obtained by MRFI.

As shown in Figures 12 and 14, axial velocity profiles at various locations along a single fiber as measured by magnetic resonance imaging correlate well with simulations from nonconcentric simplified model equations. The fit is best for images taken near the central section of the module, where axial velocities are highest, Figure 12a. Similarly, the major devia-

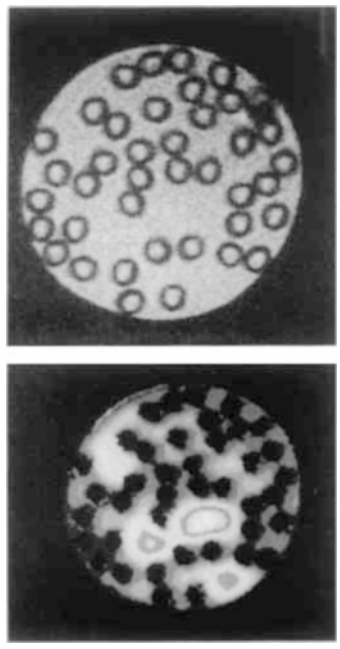

(a) no flow; (b)flow at 250 mL/min
Darker areas indicate higher velocities.

Figure 15. Multiple-fiber module: images of velocity in bioreactor.

tions from theory at a given axial location occur primarily at the lower axial velocities and higher radial velocities. In-plane radial flow can lead to a misregistration between physical location and pixel location in the image. This may explain the relatively poor correlation between the model and experimental data near the entrance of the hollow-fiber bioreactor.

The earlier assumption in the development of the model equations that diffusion is negligible compared to the convective transport should now be verified. One can calculate a Peclet number for transport in the extracapillary space as shown by the following equation:

$$Pe = \frac{v_{avg} R_2}{D_e} \tag{21}$$

where v_{avg} is the average measured velocity in the ECS at the longitudinal midpoint of the reactor, R_2 is the outer radius of the membrane, and D_e is the effective diffusivity. From the results shown in Figure 8, which represent data closest to the midpoint of the reactor, we can assign an approximate value of 0.4 cm/s to v_{avg}. The membrane has an outer radius of 0.065 cm and the diffusivity of water in water is approximately 1×10^{-5} cm^2/s. This yields a Peclet number of 2,600, confirming that diffusive transport is indeed negligible compared to convection. However, this may not always be the case, especially when the convective transport is limited by the low permeability of a densely packed cell region.

Since the axial velocity data profiles and the location of maxima are quite closely represented by the theoretical predictions, the model equations and associated assumptions have been shown to be valid in describing Starling leakage flows in hollow-fiber membrane systems. Application of the equations should now be used to suggest design and operating parameters for optimizing the effects of such flows. As an example, diffusion analysis reveals that short reactor lengths are often necessary to avoid mass transfer limitations at the distal end of a hollow-fiber system (Heath and Belfort, 1987). With the added transport by convection, the effective reactor length may be increased, although axial concentration gradients will still exist.

In a similar theoretical analysis for a radial flow bioreactor, Tharakan and Chau (1986) established guidelines for minimizing concentration gradients using nondimensional parameters. In that study they investigated parameter values for improving product separation in the module and found that the resulting constraints were in opposition to those for enhancing nutrient distribution. This further demonstrates that the effects of convective flow must be optimized for the particular requirements of different systems.

In conclusion, this analysis can be instrumental in determining reactor dimensions, flow rate, membrane characteristics, catalyst packing densities, and other factors for a variety of applications both within and beyond the field of biotechnology. The combination of magnetic resonance imaging measurements and mass transfer modeling provides a versatile method for improving design, operation, and scale-up of membrane systems for a variety of uses.

Acknowledgment

This research was supported by funds from the New York State Science and Technology Foundation, award no. SSF(87) 20 and the National Science Foundation Small Business Innovation Research Program, award no. ISI-8760455. The hollow-fiber modules were kindly supplied by Arie Gollan of A/G Technology.

Notation

A = coefficient defined in Appendix
a = spatial coordinate, Figure 2
B = coefficient defined in Appendix
C_n = coefficient defined in Appendix
D_e = effective diffusivity
$\mathbf{F}$ = body forces vector
F_i = function defined in Appendix
k = Darcy permeability
k_2 = isotropic membrane permeability
k_{21} = nonisotropic membrane permeability in r direction
k_{22} = nonisotropic membrane permeability in z direction
k_3 = permeability in extracapillary space
L = reactor length
P = pressure vector
P_O = reactor inlet pressure
P_L = reactor outlet pressure
P_1 = hydrostatic pressure in lumen
P_2 = hydrostatic pressure in membrane
P_3 = hydrostatic pressure in extracapillary space
Pe = Peclet number
Q = volumetric flow rate
$Q3$ = volumetric flow rate in extracapillary space
R = inner radius of phantom tube
R_1 = radius of lumen
R_2 = radius of lumen and membrane
R_3 = radius of lumen, membrane, and extracapillary space
r = radial coordinate
t = time
u = radial velocity
u_1 = radial velocity in lumen
u_2 = radial velocity in membrane
u_3 = radial velocity in extracapillary space
$\mathbf{V}$ = velocity vector
v = axial velocity
v_1 = axial velocity in lumen
v_2 = axial velocity in membrane

v_3 = axial velocity in extracapillary space
v_{avg} = average axial velocity in extracapillary space at longitudinal reactor midpoint
v_{max} = maximum axial velocity
X_3 = function defined in Appendix
x = spatial coordinate, Figure 2
y = spatial coordinate, Figure 2
z = axial coordinate

Greek letters

α = coefficient, Eq. 18
α_n = coefficient defined in Appendix
β = concentric inner cylinder radius in ζ plane
$\bar{\eta}$ = fluid viscosity
η = complex point of complex variable ζ
μ = off-center displacement of fiber in cartridge
ν = fluid kinematic viscosity
ρ = fluid density
ξ = real part of complex variable ζ
ζ = transformation function, Eq. 18

Literature Cited

Apelblat, A., A. Katzir-Katchalsky, and A. Silberberg, "A Mathematical Analysis of Capillary-Tissue Fluid Exchange,"*Biorheol.* **11,** 1 (1974).

Belfort, G., "Membranes and Bioreactors: A Technical Challenge in Biotechnology," *Biotech. Bioeng.*, **33,** 1047 (1989).

Davis, M. E., and L. T. Watson, "Analysis of a Diffusion-Limited Hollow-Fiber Bioreactor for the Measurement of Effective Substrate Diffusivities," *Biotech. Bioeng.*, **27,** 182 (1985).

———, "Mathematical Modeling of Annular Reactors," *Chem. Eng. J.*, **33,** 133 (1986).

Edelstein, W. A., J. M. S. Hutchinson, G. Johnson, and T. Redpath, "Spin Warp NMR Imaging and Applications to Human Whole-Body Imaging," *Phys. Med. Biol.*, **25,** 751 (1980).

Georgakis, C., P. C. H. Chan, and R. Aris, "The Design of Stirred Reactors with Hollow-Fiber Catalysts for Michaelis-Menten Kinetics," *Biotech. Bioeng.*, **17,** 99 (1975).

Heath, C. A., "Engineering Aspects of Improved Antibody Production by Hybridomas," Ph.D. Thesis, Rensselaer Polytech. Inst., Troy, NY (1988).

Heath, C. A., and G. Belfort, "Immobilization of Suspended Mammalian Cells: Analysis of Hollow-Fiber and Microcapsule Bioreactors," *Adv. Biochem. Eng./Biotech.*, **34,** 1 (1987).

Horvath, C., L. H. Shendalman, and R. T. Light, "Open Tubular Heterogeneous Enzyme Reactors: Analysis of a Theoretical Model," *Chem. Eng. J.*, **28,** 375 (1973).

Karel, S. F., and C. R. Robertson, "Reaction Rate Calculations for Cosubstrates Diffusing into Catalyst Layer from Opposite Sides," *Biotech. Bioeng.*, **30,** 427 (1987).

Kim S., and D. O. Cooney, "An Improved Theoretical Model for Hollow-Fiber Enzyme Reactors," *Chem. Eng. Sci.*, **31,** 289 (1976).

Knight, P., "Hollow-Fiber Bioreactors for Mammalian Cells," *Bio/Technology*, 7(5) 459 (1989).

Moran, P. R., "A Flow Velocity Zeugmatographic Interlace for NMR Imaging in Humans, Hollow-Fiber Bioreactors for Mammalian Cell Culture," *Magn. Reson. Imag.*, **1,** 197 (1982).

Nishimura, D. G., A. Macovski, and J. M. Pauly, "Magnetic Resonance Angiography," *IEEE Trans. Med. Imag.*, **MI-5,** 140 (1986).

Rony, P. R., "Multiphase Catalysis. II: Hollow-Fiber Catalysts," *Biotech. Bioeng.*, **13,** 431 (1971).

Salmon, P. M., S. B. Libicki, and C. R. Robertson, "A Theoretical Investigation of Convective Transport in the Hollow-Fiber Reactor," *Chem. Eng. Comm.*, **66,** 221 (1988).

Schonberg, J. A., and G. Belfort, "Enhanced Nutrient Transport in Hollow-Fiber Perfusion Bioreactors: A Theoretical Analysis," *Biotech. Prog.*, **3,** 80 (1987).

Shuler, M. L., "Immobilization of Cells by Entrapment in Membrane Bioreactors," *Meth. Enzym.*, **135,** 372 (1987).

Starling, E. H., "On the Absorption of Fluid from the Connective Tissue Spaces," *J. Physiol.*, **19,** 312 (1896).

Tharakan, J. P., and P. C. Chau, "Operation and Pressure Distribution of Immobilized Cell Hollow-Fiber Bioreactors," *Biotech. Bioeng.*, **29,** 657 (1986).

Waterland, L. R., A. S. Michaels, and C. R. Robertson, "A Theoretical Model for Enzymatic Catalysis Using Asymmetric Hollow-Fiber Membranes," *AIChE J.*, **20,** 50 (1974).

Webster, I. A., and M. L. Shuler, "Mathematical Models for Hollow-Fiber Enzyme Reactors," *Biotech. Bioeng.*, **20,** 1541 (1978).

———, "Whole-Cell Hollow-Fiber Reactor: Transient Substrate Concentration Profiles," *Biotech. Bioeng.*, **23,** 447 (1981).

Webster, I. A., M. L. Shuler, and P. R. Rony, "Whole-Cell Hollow-Fiber Reactor: Effectiveness Factors," *Biotech. Bioeng.*, **21,** 1725 (1979).

Appendix

Solution of text Eqs. 4–11 for a hollow-fiber system (after Apelblat et al., 1974).

For the fiber lumens:

$$P_1(z) = A + B\left[z - \sum_{n=1}^{\infty} \frac{C_n D_n}{\alpha_n} \cos(\alpha_n x)\right] \tag{A1}$$

$$u_1(r, z) = \frac{1}{16\bar{\eta}} \frac{d^2P}{dz^2} (2rR_1^2 - r^3) \tag{A2}$$

$$v_1(r, z) = \frac{1}{4\bar{\eta}} \frac{dP}{dz} (r^2 - R_1^2) \tag{A3}$$

For the membrane (isotropic) and extra capillary regions ($i = 2, 3$):

$$P_i(r, z) = A + B\left[L/2 + \sum_{n=1}^{\infty} C_n F_i(\alpha_n r) \cos(\alpha_n z)\right] \tag{15}$$

$$u_i(r, z) = -\frac{k_i}{\bar{\eta}} \frac{\partial P_i}{\partial r} \tag{13,14}$$

$$v_2(r, z) = -\frac{k_{22}}{\bar{\eta}} \frac{\partial P_2}{\partial z} \tag{12}$$

$$F_2(\alpha_n r) = W_n I_0(\alpha_n r) + S_n K_0(\alpha_n r) \tag{A4}$$

$$F_3(\alpha_n r) = K_0(\alpha_n r) + K_1(\alpha_n R_3) I_0(\alpha_n r)/I_0(\alpha_n R_3) \tag{A5}$$

where

$$\alpha_n = n\pi/L$$

$$A = P_0 + B \sum_{n=1}^{\infty} \frac{C_n D_n}{\alpha_n}$$

$$B = \frac{P_L - P_0}{L - \epsilon}$$

$$C_n = \frac{2[(-1)^n - 1]}{\alpha_n L(D_n + \alpha_n J_n)}$$

$$D_n = \frac{16k_2}{R_1^3} [S_n K_1(\alpha_n R_1) - W_n I_1(\alpha_n R_1)]$$

$$F_2(\alpha_n r) = W_n I_0(\alpha_n r) + S_n K_0(\alpha_n r)$$

$$F_3(\alpha_n r) = K_0(\alpha_n r) + K_1(\alpha_n R_3) I_0(\alpha_n r)/I_0(\alpha_n R_3)$$

$$G_n = K_1(\alpha_n R_3) I_0(\alpha_n R_2)/I_1(\alpha_n R_3) + K_0(\alpha_n R_2)$$

$$H_n = K_1(\alpha_n R_3) I_1(\alpha_n R_2)/I_1(\alpha_n R_3) - K_1(\alpha_n R_2)$$

$$J_n = W_n I_0(\alpha_n R_1) + S_n K_0(\alpha_n R_1)$$

$$S_n = \alpha_n R_2 [G_n I_1(\alpha_n R_2) - H_n I_0(\alpha_n R_2) k_3/k_2]$$

$$W_n = \alpha_n R_2 [G_n K_1(\alpha_n R_2) + H_n I_0(\alpha_n R_2) k_3/k_2]$$

$$\epsilon = \sum_{n=1}^{\infty} \frac{C_n D_n}{\alpha_n} [(-1)^n - 1]$$

$$\lambda = R_1/R_3$$

where I and K are modified Bessel functions of the first and second kinds, respectively, and the subscript (0 or 1) indicates the function order.

The streamlines for the extracapillary region are given by

$$\Psi_3(r, z) = 2\pi r B \sum_{n=1}^{\infty} C_n X_3(\alpha_n r) \sin(\alpha_n z) \tag{A6}$$

$$X_3(\alpha_n r) = K_1(\alpha_n R_3) I_1(\alpha_n r)/I_1(\alpha_n R_3) - K_1(\alpha_n r) \tag{A7}$$

The lumen and leakage (into the extra capillary region) flows are given by

$$Q_1 = -\frac{\pi R_1^4 B}{8\bar{\eta}} \tag{A8}$$

$$Q_3(z) = -\frac{2\pi R_2 k_3 B}{\bar{\eta}} \sum_{n=1}^{\infty} C_n X_3(\alpha_n R_2) \sin(\alpha_n z) \tag{16}$$

Manuscript received July 28, 1989, and revision received Jan. 16, 1990.